Bed form initiation from a flat sand bed

Jeremy G. Venditti[1,2] and Michael A. Church
Department of Geography, University of British Columbia, Vancouver, British Columbia, Canada

Sean J. Bennett
Department of Geography, University at Buffalo, Buffalo, New York, USA

Received 11 March 2004; revised 13 August 2004; accepted 2 November 2004; published 16 February 2005.

[1] Bed form initiation in unidirectional flow is examined on a flat bed composed of a homogeneous 0.5 mm sand. Velocity profiles taken prior to bed form development indicate that the examined flows are typical of fully turbulent, uniform, open channel flows. Under these conditions, two separate modes of bed form initiation are observed: defect and instantaneous initiation. Defect initiation occurs at lower flow stages, where sediment transport is sporadic and patchy, and is characterized by defect propagation associated with flow separation. Instantaneous initiation occurs at larger flow strengths, where sediment transport is general and widespread. This form of bed form initiation begins with the imprinting of a cross-hatch pattern on the flat sediment bed, which leads to chevron-shaped forms that migrate independently of the initial pattern. The chevrons eventually align to form incipient crest lines. This mode of bed form initiation does not appear to be linked to turbulent structures, but integral scales derived from velocity measurements prior to bed form development are similar to the initial bed form length scales.

Citation: Venditti, J. G., M. A. Church, and S. J. Bennett (2005), Bed form initiation from a flat sand bed, *J. Geophys. Res.*, *110*, F01009, doi:10.1029/2004JF000149.

1. Introduction

[2] The origin of bed forms developed in unidirectional flow has fascinated researchers from many disciplines and yet, in spite of nearly a century of effort, there exists no comprehensive theory capable of describing the spectrum of observed shapes and sizes [*Raudkivi*, 1997]. Over the last 50 years, most work on bed form development has focused on one of two theories: 1) linear stability (perturbation) theory and the response of a flat bed to a sinusoidal perturbation and 2) the formation and propagation of bed defects. Initially proposed by Felix M. Exner in the 1920s (as described by *Leliavsky* [1955]) and later developed by *Anderson* [1953], perturbation theory involves the linearization of the equations of motion of both fluid and sediment over a bed perturbation or defect to predict suppression or growth of the perturbation [*McLean*, 1990]. It is proposed that the initial instability results from a phase difference between the maximum bed load transport rate and the bed topography, and a number of mechanisms have been proposed for the lag [cf. *Kennedy*, 1963; *Smith*, 1970; *Engelund*, 1970; *Fredsoe*, 1974]. However, there is no insight into the origin of the perturbation.

[3] More recent work has surmised that bed forms are developed from defects in the sand bed which are propagated downstream by flow separation mechanisms [*Raudkivi*, 1963, 1966]. It has been proposed that the origin of the defects is linked to coherent turbulent flow structures [*Williams and Kemp*, 1971; *Best*, 1992]. In particular, microturbulent sweeps, which are part of the bursting process that is ubiquitous in flow over smooth surfaces, are envisioned to create flow parallel ridges which flare at their downstream ends, creating small accumulations of sediment or "defects" [*Best*, 1992]. However, there is a large temporal- and spatial-scale transition between microturbulent bursts and the organization of a sand bed. Furthermore, microturbulent bursts are typically random and it is not clear how bed forms, which are one of the most regular natural features on Earth's surface, can result from a spatially and temporally random process. These criticisms are complemented by the observation of bed form development in laminar flows [*Kuru et al.*, 1995; *Coleman and Eling*, 2000]. In fact, *Kuru et al.* [1995] found no significant change in the bed form initiation mechanisms across the transition to turbulent flow.

[4] In this paper, bed form initiation from a flat sand bed is examined with and without artificially generated bed defects (small indentations or mounds of sediment). A series of grain movements and bed deformations are documented that lead to incipient bed form crest lines and linkages are

[1]Now at Department of Earth and Planetary Sciences, University of California, Berkeley, California, USA.
[2]Also at Stillwater Sciences, Berkeley, California, USA.

0148-0227/05/2004JF000149$09.00

Table 1. Summary of Flow Parameters[a]

Flow Parameter	Flow A	Flow B	Flow C	Flow D	Flow E
d, m	0.152	0.152	0.153	0.153	0.153
$\bar{U}$, m s^{-1}	0.501	0.477	0.454	0.399	0.356
U_{max}, m s^{-1}	0.593	0.559	0.537	0.456	0.401
Fr	0.411	0.391	0.370	0.326	0.290
Re	75936	72331	69568	61093	54580
Q, m^3 s^{-1}	0.0759	0.0723	0.0696	0.0611	0.0546
$S_{t=0} \times 10^{-4}$	12	11	7	5.5	5.5
Determinations Based on Linear Portion of the Vertical Reynolds Stress Profile					
u_{*R}, m s^{-1}	0.028	n/a	0.025	0.019	0.019
τ_R, Pa	0.763	n/a	0.637	0.341	0.350
Determinations Based on Reynolds Stress Measured at 5 mm Above Bed (10 min Average)					
u_{*B}, m s^{-1}	0.027	0.028	0.022	0.018	0.012
τ_B, Pa	0.718	0.782	0.469	0.311	0.135
Determinations Based on Law of the Wall Using Lower 20% of Averaged Profile					
$u_{*0.2}$, m s^{-1}	0.030	0.026	0.022	0.017	0.016
$\tau_{0.2}$, Pa	0.902	0.650	0.481	0.291	0.242
$z_{o0.2}$, mm	0.084	0.044	0.023	0.008	0.006
$k_{s0.2}$, mm	2.53	1.32	0.68	0.23	0.19
$\widetilde{ff}_{0.2}$	0.029	0.023	0.019	0.015	0.015
Re_g	15.0	13.0	11.0	8.5	8.0

[a] $Fr = \bar{U}/(gd)^{0.5}$, $Re = d\bar{U}/\nu$, $k_s = 30.2z_o$, $ff = 8\tau/(\rho\bar{U}^2)$, $u_* = (\tau/\rho_w)^{0.5}$, $Re_g = Du_{*0.2}/\nu$.

made to properties of the flow structure. The initial flow conditions, prior to bed form development, are investigated first in order to establish that the flow agrees with standard models of flow and turbulence over hydraulically rough, flat beds.

2. Experimental Procedures

[5] The experiments were conducted at the National Sedimentation Laboratory, United States Department of Agriculture, Oxford, Mississippi, using a tilting, recirculating flume 15.2 m long, 1 m wide, and 0.30 m deep, that recirculates both sediment and water. The flume was filled with ~2250 kg of narrowly graded, unimodal, washed and sieved white quartz sand with a median grain size D_{50} = 0.5 mm.

[6] Bed form development was observed over five separate flow stages (referred to as flows A–E (Table 1)). Flow depth d was ~0.15 m and mean flow velocities ($\bar{U} = Q/(y_w d)$ where y_w is the flume width) ranged between 0.36 and 0.50 m s^{-1}. Froude and Reynolds numbers indicate that the flow was both subcritical and fully turbulent (see Table 1). These five flow stages were selected to provide a test of similarity among the observations over a range of hydraulic conditions.

[7] Runs were ~12 hours long, but only the initiation portions of the runs, lasting between 5 min and 1 hour, are discussed here. At the beginning of each experimental run, the sediment bed was artificially flattened using a 38 mm piece of aluminum angle mounted across the flume, at bed level, on a cart that traveled the length of the flume. This removed all variation in the bed greater than 1 mm. Flattening was done in several centimeters of water with the flume pump off. The flume was then carefully filled to 0.15 m. Flow in the flume modified this flow depth and established the water surface slope S which was monitored using two ultrasonic water level probes along 2.25 m of the flume.

2.1. Video

[8] The development of the sand bed was monitored using a high-resolution (Super-VHS) video camera mounted above the flume and centered at ~10.3 m from the head box. The video was focused to capture an area of the bed 0.8 × 0.9 m. The video was illuminated with four 100 W floodlights mounted on the flume sidewalls and oriented to intersect at the camera focal point. The side lighting produced a glare-free image with light shadows that highlighted millimeter-scale changes in the bed structure. The video records were subsampled from the tapes using a frame grabber at intervals that ranged between 1 and 10 s to produce a series of images that were further analyzed to determine morphologic changes in the sand bed over time.

[9] All measurements taken from these images were made in reference to a grid with 0.1 m squares, installed at the height of the flume walls in the video view. Since the video camera was focused at the bed, which was ~0.4 m below the grid, features observed on the bed were actually larger than they appeared relative to the grid. A 0.1 m square was placed at several locations on the bed to estimate the correction factors necessary to obtain actual lengths and areas. The measurements indicated that all areas needed to be multiplied by 1.28 and all lengths needed to be multiplied by 1.15. The necessary correction for measured lines should be the square root of the distortion in the area (i.e., $\sqrt{1.28} = 1.13$ or 13%). The difference between the observed and expected distortion is caused by the spatial variation in the areas and sides of the squares that make up the grid. The measured distortion is used for corrections. Further information about this correction can be found in *Venditti* [2003].

[10] Analysis of the radial distortion caused by the spherical aberration of the camera showed there is a linear

distortion of ~2% (areal distortion of ~4%) from the center of the image to the outer edges. However, this is less than the spatial variation in the line lengths (and areas) that make up the grid [*Venditti*, 2003]. Thus no corrections were applied.

2.2. Echo Soundings

[11] In addition to the video, the bed surface topography was digitized using two acoustic echo sounders built by the National Center for Physical Acoustics (NCPA) at the University of Mississippi. The sensors had a nominal resolution (0.05 mm) much less than the grain size in the experiments, which was their practical resolution. The sensors were mounted with a cross-stream separation of 0.45 m on a computer-controlled cart driven upstream and downstream by a stepper motor, gear reducer and a sprocket riding on a chain on the flume sidewall. The cart was also fitted with a ball screw axis, driven by stepper motors, which allowed instruments to be positioned in the cross-stream direction. The motion control system was programmed so that the sensors could be moved: (1) across the flume 0.45 m, (2) downstream 5 mm, (3) across the flume in the opposite direction and (4) downstream 5 mm. This motion was then repeated to pass sensors over the area of interest providing a data grid with a spatial resolution of ~5 mm. Mapping was done before each run to ensure the planar nature of the bed and at ~1 hour intervals throughout the experiments. Subsequent analysis of the grids indicated that at the greatest three flow strengths (A, B and C) the rates of bed form development and migration were too fast to provide any useful information (i.e., the bed forms appeared distorted in the maps). In contrast, at the lowest two flow strengths, development was sufficiently slow so that distortion was quite minimal and the full developmental process could be monitored.

2.3. Flow Velocity Data

[12] Velocity profiles were obtained for all five flow stages over an initially flat bed using a 300 mW Dantec laser-Doppler anemometer (LDA) operated in backscatter mode with burst-type detectors. The LDA measures two-component flow velocities (u and w) has a reported precision of ±0.1 mm s^{-1}, a focal length of 750 mm and a sampling volume of 10 × 1 × 1 mm [*Dantec Measurement Technology*, 1995]. Positive velocity components were downstream and up. The flow was seeded with silica flour that was typically less than 20 μm in diameter. Data were acquired at 20 Hz near the bed, and up to 1 kHz in the upper part of the profiles when velocity measurements were collected coincidentally. Much larger sampling frequencies were achieved when velocity components were measured independently of each other. Measurements with a sampling frequency less than 20 Hz were discarded.

[13] The laser was positioned by a three axis motion control system that allowed the probe head to be adjusted quickly to within fractions of a millimeter. The motion control system was set so that the measuring volume was normal to the flume wall and offset 4° from the vertical plane. This allowed the measuring volume to be placed in the center of the flume, 5 mm above the bed, while still measuring velocity data on both components.

[14] The velocity profiles were composed of 60 s samples collected at 15 points in the vertical plane. The sampling period could not be extended as the bed developed too quickly. Two sets of profiles were taken to ensure consistent results within the short sampling period. Each set consists of a profile at each flow strength. In profile set 2, an additional velocity profile was taken at the largest flow strength (A) as the bed developed rapidly. At the larger flow strengths (A, B, C) sand waves developed as the upper portions of the profiles were measured. However, these features were less then a few mm in height and should not have significantly affected the profiles away from the bed. Water surface slope was not significantly affected. As the bed forms grew, there were more significant changes in the water surface slope and hence the velocity profiles. There was no topography when measurements were being taken near the bed.

[15] Profiles were also acquired over artificially made bed defects, mounds or pits in the flat bed, at the two lowest flow strengths. At the beginning of the second set of profiles, a 600 s velocity sample was taken at 5 mm above the flat bed. These long time series were used to examine integral scales of flow and to provide accurate estimates of the near–bed flow properties.

3. Initial Flow Structure

[16] Before discussing the initial bed features, it is necessary to discuss the structure of the flow that was present as these features were initiated in order to establish that the initiation processes were not occurring under some aberrant flow condition.

3.1. Velocity Profile Data Analysis

[17] Time-averaged at-a-point streamwise U and vertical W velocities were calculated as

$$U = \frac{1}{n}\sum_{i=1}^{n} u_i \qquad W = \frac{1}{n}\sum_{i=1}^{n} w_i, \tag{1}$$

where u_i and w_i are instantaneous velocities and n is the total number of measurements. The mean streamwise velocity $\overline{U}$ of a roughly logarithmic velocity profile is U at 0.36 d. Root-mean-square (rms) streamwise velocity U_{rms} was calculated from

$$U_{\mathrm{rms}} = \left[\frac{1}{n}\sum_{i=1}^{n}(u_i - U)^2\right]^{0.5}. \tag{2}$$

The Reynolds shear stress τ_{uw} was determined using

$$\overline{u'w'} = \frac{1}{n}\sum_{i=1}^{n}(u_i - U)(w_i - W) \tag{3}$$

$$\tau_{uw} = -\rho_w \overline{u'w'}, \tag{4}$$

where ρ_w is the fluid density.

[18] The boundary shear stress was estimated for each profile using three methods. The first method is based on the von Karman-Prandtl law of the wall. At-a-point U velocities were plotted as a function of height above the bed z and least squares regression was used to determine the

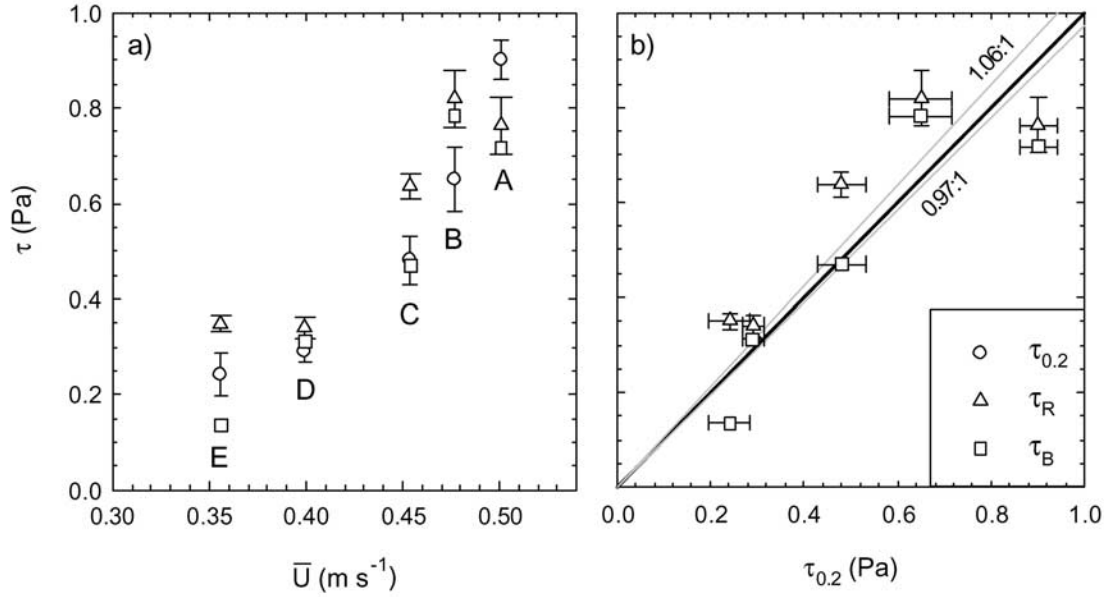

Figure 1. Measures of boundary shear stress τ plotted against (a) velocity U and (b) the shear stress estimate based on the law of the wall, $\tau_{0.2}$. Values of τ_R are based on the Reynolds stress profile, and values of τ_B are based on the Reynolds stress measured at 5 mm above the bed. Error bars are the standard error of the estimate from the regressions used to calculate $\tau_{0.2}$ and τ_R. Displayed results are based on the combined measured profiles for $\tau_{0.2}$ and τ_R.

roughness height z_o as the z intercept. The shear velocity was calculated from

$$\frac{U}{u_*} = \frac{1}{\kappa} \ln \frac{z}{z_o}, \tag{5}$$

where U is the mean velocity at height z and κ is the von Karman constant, which is assumed to be 0.4. The law of the wall is strictly applicable only to the log-layer where the increase in U with z is logarithmic. In fully turbulent open channel flow, this region extends from a few mm above the bed to $0.2d$ [*Nezu and Nakagawa*, 1993]. Accordingly, equation (5) was applied to only the lower 20% of each profile. The boundary shear stress based on the law of the wall (denoted $\tau_{0.2}$) is determined from

$$\tau = \rho_w u_*^2. \tag{6}$$

[19] The second method uses vertical profiles of τ_{uw}. For uniform flows without bed forms,

$$\tau_{uw} = \tau_R(1 - z/d). \tag{7}$$

An estimate of τ_R can be obtained by using a least squares regression projected to $z/d = 0$ [see *Nezu and Rodi*, 1986; *Lyn*, 1993]. The third method uses a near bed measurement of τ_{uw} (denoted τ_B) [cf. *Nelson et al.*, 1995] at 5 mm above the bed, which is well above the transport layer. In these experiments, the 600 s u and w velocity measurements at 5 mm above the bed were used to determine τ_B using equations (3) and (4) and u_* using equation (6).

3.2. Boundary Shear Stress

[20] The mean and rms velocities as well as the covariances were averaged for points measured at the same height during different profiles for each flow stage to produce more robust estimates of each quantity. Only profile points with two or three measurements available were averaged. At some locations near the bed, the sampling frequency for τ_{uw} values dropped below 20 Hz and were not included in the profile regressions so τ_{uw} profiles are truncated at $\sim 0.2\ d$. The combined U and τ_{uw} profiles produced a consistent increase in $\tau_{0.2}$ and τ_R with flow strength (Figure 1a) except at flow B where the τ_R value was inconsistent with the general pattern after the averaging. This point is removed from further consideration.

[21] By examining the increase in τ_B as well as combined values of $\tau_{0.2}$ and τ_R, it is clear that, regardless of which calculation is used, the boundary shear stress increase with $\overline{U}$ is nonlinear (Figure 1a). The boundary shear is nearly the same at flow strengths D and E while from A to C the increase with $\overline{U}$ is more pronounced. Figure 1b displays the boundary shear stress plotted against $\tau_{0.2}$ for combined profiles which shows $\tau_{0.2} \approx \tau_R \approx \tau_B$. This suggests that the flow does not differ significantly from other documented uniform flows.

3.3. Mean and Turbulent Flow

[22] Table 1 summarizes the flow conditions from the experiments based on the combined velocity and stress profiles (including values based on τ_B). The roughness height is variable depending on which method is used to determine the boundary shear stress; $z_{o0.2}$ ranged between 0.006 and 0.084 mm with an associated error (2 times the standard error) that ranged between 0.004 and 0.038 mm. Equivalent sand roughness values k_s, determined from

$$k_s = 30.2 z_o, \tag{8}$$

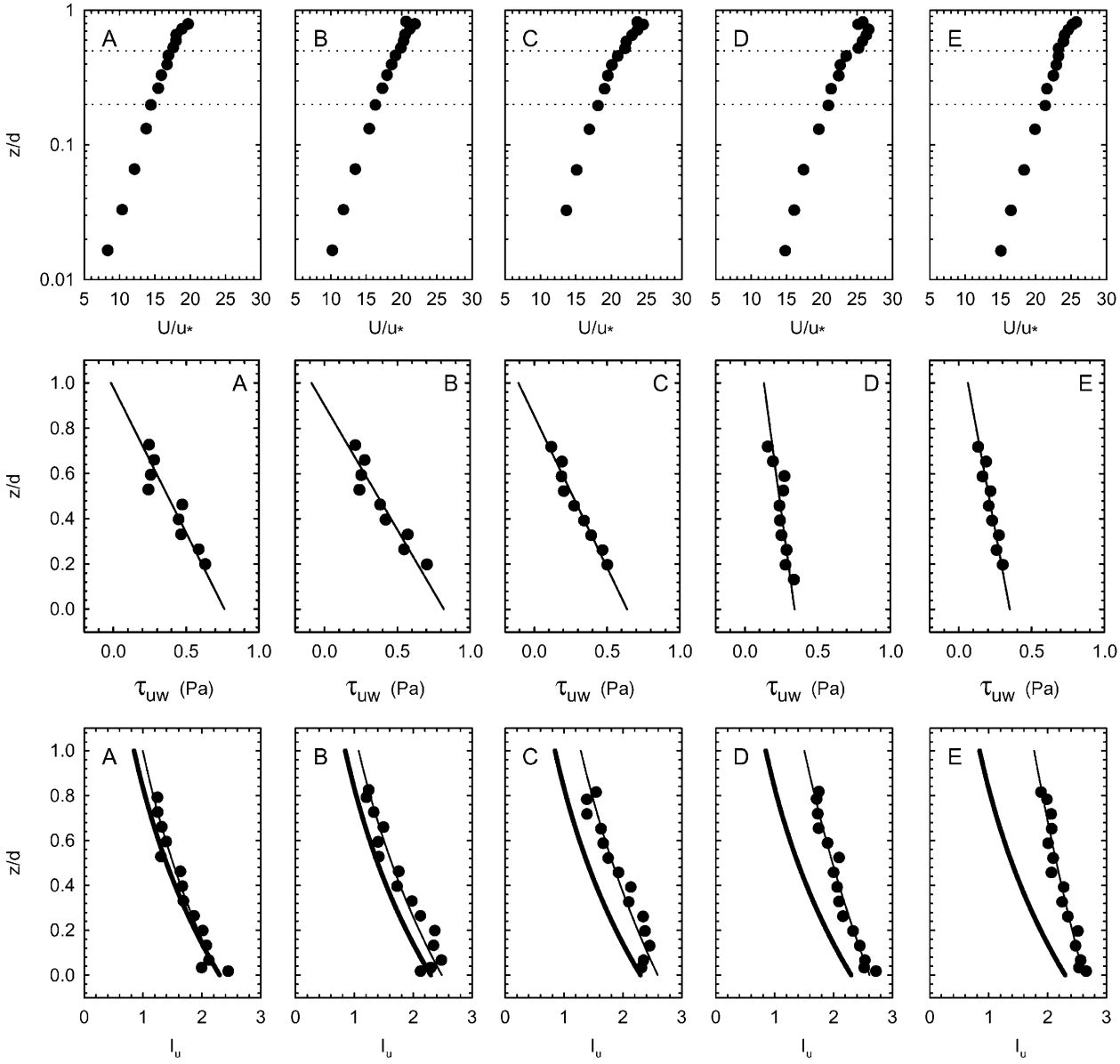

Figure 2. Profiles of mean streamwise velocity U, streamwise turbulence intensity I_u, and Reynolds shear stress τ_{uw}. Letters A–E refer to the flow strengths (see Table 1). U is normalized by shear velocity u_*, calculated using the von Karman-Prandtl law of the wall. Height above the bed z is normalized by the flow depth d. Thick lines in the bottom panels are *Nezu and Nakagawa*'s [1993] universal turbulence intensity function (equation (10)) plotted using their coefficients. Thin lines are *Nezu and Nakagawa*'s [1993] function plotted using coefficients determined from least squares regressions that are provided in Table 2.

[*van Rijn*, 1993] range between 0.19 and 2.53 mm using $\tau_{0.2}$. *Yalin* [1992] suggests $k_s \approx 2D$ based on experiments with movable yet stationary grains. This relation yields $k_s \approx$ 1.0 mm, which is within the range of observed k_s values. However, the range in k_s suggests that the flow responds to locally variable aggregations of grains rather than to individual grain characteristics.

[23] The combined U profiles are presented in the top panels of Figure 2. The velocity profiles are essentially linear through the lower 0.2 d, but there is a kink in the upper portion of the profiles at ~0.5 d. This outcome is not surprising as the profiles are expected to be linear only through the log-layer, which is generally accepted to extend from a few mm above the bed to 0.2 d [*Nezu and Nakagawa*, 1993]. The combined τ_{uw} profiles also appear in Figure 2 (middle) and show a linear decrease with z, as is expected for uniform flow.

[24] The u turbulence intensities, calculated from

$$I_u = \frac{U_{\mathrm{rms}}}{u_{*0.2}}, \tag{9}$$

Table 2. Values of Parameters in Equation (10) Evaluated From Measured Profiles

Flow	D_u	C_{ku}
Nezu and Nakagawa	2.30	1.0
A	2.28	0.83
B	2.49	0.84
C	2.59	0.70
D	2.61	0.55
E	2.61	0.39
Mean	2.52	0.66

are plotted in Figure 2 (bottom). Also plotted is the semitheoretical, universal function for turbulent intensity provided by *Nezu and Nakagawa* [1993], calculated as

$$I_u = D_u \exp(-C_{ku} z/d), \tag{10}$$

where D_u and C_{ku} are empirical constants. These have been previously determined experimentally for laboratory open channel flows as 2.30 and 1.0 respectively [*Nezu and Nakagawa*, 1993]. These values are not universal constants but depend on bed roughness and the presence of bed forms. For example, *Sukhodolov et al.* [1998] calculated a new set of constants for flow over a bed form field that were somewhat different from those provided above. In consideration of this, a new set of constants was calculated using least squares regression for the flows in these experiments (Table 2) which are similar to those calculated by *Nezu and Nakagawa* [1993].

[25] Overall, the velocity data suggest that flow over the lower-stage plane beds at the beginning of the experiments is in accordance with conventional models of uniform flow over flat beds [e.g., *Nezu and Nakagawa*, 1993]. Estimates of the boundary shear stress derived from different methods are similar in magnitude and increase in a similar fashion with $\overline{U}$. Values of equivalent sand roughness are consistent with previous observations. The turbulence intensities can be modeled by the semiempirical functions of *Nezu and Nakagawa* [1993], provided that they are recalibrated for the varying flow strengths, and the momentum exchange (τ_{uw}) conforms with current formulations for fully turbulent, uniform, open channel flows over flat beds.

4. Modes of Bed Form Initiation

[26] Two modes of bed form initiation were observed in the experiments: defect initiation and instantaneous initiation. At the two lowest flow strengths used in the experiments (D and E), a flat bed appears to be stable for long periods of time, even though sand movement indicated the threshold of motion had been exceeded. Sediment transport at these flow stages was patchy and sporadic. Many early researchers [e.g., *Menard*, 1950; *Simons and Richardson*, 1961; *Raudkivi*, 1963] have suggested that any sediment motion on a flat bed will lead to bed form development. However, others [*Liu*, 1957; *Bogardi*, 1959; *Southard and Dingler*, 1971] have reported stable flat beds with sediment transport and no bed form development. The flat beds observed here could not be maintained indefinitely. Sediment carried into the head box was ultimately deposited at the entrance to the channel and developed small mounds of sediment. Eventually, these mounds of sediment developed into bed form trains that propagated through the flume channel. At flow strength E the bed form fields took nearly 3 hours to migrate from the head box to the area where observations were being made (~9.8 m). At the second lowest flow strength (D) the bed form fields took ~35–45 min to migrate the same distance. As the bed was flattened, millimeter-scale indentations or mounds of sediment (defects) formed at the sidewalls or in the channel, albeit infrequently. At flow strength D, these defects occasionally propagated downstream forming bed form fields. Interestingly, not all defects developed into bed forms. If sediment entering the flume did not form mounds, it is possible that the stable flat beds could have existed indefinitely.

[27] In contrast to this type of bed form development, at the greater flow strengths continuous and widespread sediment transport occurred and bed forms were observed to develop instantaneously over the entire bed. This type of development occurred within a few tens of seconds, with the initial appearance of the pattern that leads to bed form crest lines appearing after only a few seconds of flow. Hence this type of bed form development cannot be linked to defect propagation from the head box or sidewalls. In fact, where defects were observed on the flat bed, they were washed away as the initial bed form pattern was imprinted on the bed.

[28] The threshold between the two types of initiation was just above $\tau_{0.2} = 0.29$ Pa. A practical threshold for the sand used in these experiments occurs at $\tau_{0.2} \approx 0.30$ Pa, which corresponds to a dimensionless shear stress

$$\theta = \frac{\tau_{0.2}}{gD(\rho_s - \rho_w)} = 0.0371, \tag{11}$$

where D is the grain size (0.5 mm) and ρ_s is the grain density (2650 kg m^3). Both types of initiation, which are examined in greater detail below, occurred under hydraulic conditions that are just above the threshold for hydraulically smooth beds (i.e., transitionally rough). On the basis of a u_* value from the Inman entrainment curve [cf. *Miller et al.*, 1977], the critical θ value for entrainment of this sediment is 0.035.

[29] Before proceeding with a discussion of these bed form initiation types, it is useful to note that once established, bed forms grew exponentially in height H and length L toward an equilibrium that was reached at ~1.5 hours (Figure 3) regardless of whether the bed forms were initiated instantaneously or by defects. Average equilibrium H varies between 19.7 and 47.7 mm and average equilibrium L varied between 1.2 m and 0.3 m. Both equilibrium H and L increased with increasing flow strength [*Venditti*, 2003].

5. Defect Initiation Processes

[30] Following the work of *Southard and Dingler* [1971], who examined ripple propagation behind positive defects (mounds) on flat sand beds, the defect type of bed form development was examined from artificially made defects rather than examining bed form growth from random features on the bed. Since it seems likely that negative defects (divots) are also of interest in terms of bed form

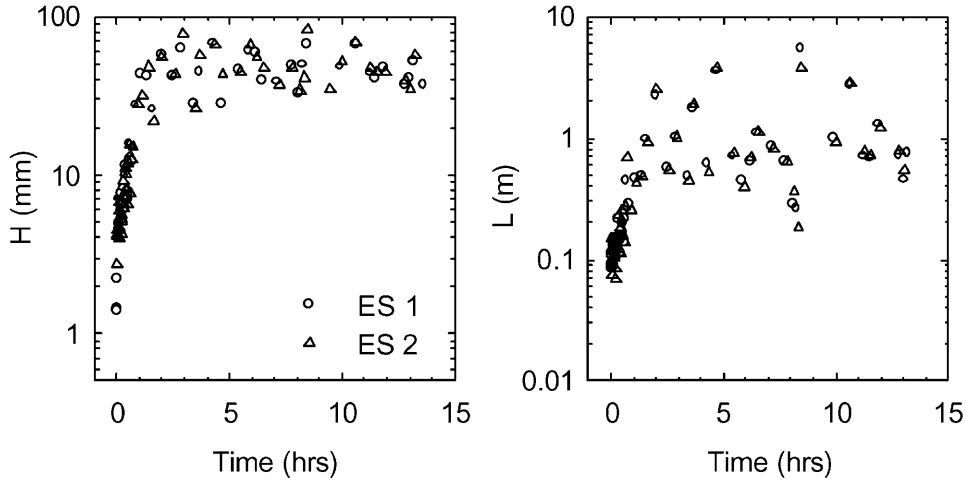

Figure 3. Typical bed form growth curves for height H and length L at flow A. Data are drawn from two echo sounders (ES1 and ES2) located in the center of the channel ~10.3 m from the head box and separated by 0.132 m. The difference in the arrival time of a bed form slip face at the echo sounders was used to calculate the bed form migration rate. L is the product of the time it took a bed form to pass an echo sounder and the migration rate. Data for flows B, C, D, and E can be found in *Venditti* [2003].

development, both positive and negative bed defects were used in the experiments herein. Defects were generated by either removing sand into or depositing sand from a large dropper until the desired defect size and cone shape were attained. Their dimensions in the runs discussed below are given in Table 3. *Southard and Dingler* [1971] noted that there was some effect of mound height on the development of ripples in their experiments. However, this conclusion is drawn from experiments using defects that varied in height between 2.5 and 50 mm. The effect of the variations in defect size here is probably insignificant.

[31] The defects used in this experiment were quite large compared to those that would typically develop from turbulent flow structures in open channel flows. *Southard and Dingler* [1971] noted that there is a threshold shear stress that must be exceeded for a defect to propagate and that this threshold decreases as the defect's height increases. Small defects (order a few millimeters), that would be expected to arise from microturbulent flow structures, did not consistently produce bed form fields, hence the choice of the larger defect size for the present experiments.

[32] The basic development pattern of the bed form fields can be observed in a series of bed maps displayed in Figure 4. Although maps were generated for positive and negative defects at flow strengths D and E, they were qualitatively similar at the coarse scale afforded by the bed mapping, therefore, only one bed form field development sequence is displayed. Figure 5 displays the bed height along the centerline of the bed form field in Figure 4. The first bed form map was taken without any flow and simply shows the positive defect (Figure 4a). The planar nature of the bed and the defect shape are evident in cross section (Figure 5), along with millimeter-scale minor asperities that did not prompt bed deformation. Subsequent maps (Figures 4b–4d) display the defect propagating downstream and developing new crests. The initial defect grew in height H and length L with each bed map, while the rest of the field is composed of bed forms that decrease in H, and L, with distance downstream (Figure 5). As the bed form propagation progressed downstream, the bed form field widened at a regular rate until it reached the sidewalls, forming a triangular shape with the initial defect at its pinnacle (Figure 4e). In cross section the bed forms began to take on a uniform H and L (Figure 5e). The map in Figure 4f shows the triangular field continuing to modify the bed, forming larger bed forms. It also shows bed forms developed at the inlet to the flume, traveling into the mapped area (~3 hours into the run) and merging with the defect bed form field. This is particularly evident in cross section where the lead bed forms generated from the head box are much smaller than those in the defect field. In the next bed map (Figure 4g) the two bed form fields have merged, but the defect field is still identifiable as larger bed forms. With subsequent bed mappings, the bed form field continues to merge and there is increasingly little observable effect of the original defect pattern (Figures 4g–4i and Figure 5). The run was extended until equilibrium H and L were reached for this flow strength (Figure 4j).

Table 3. Defect Dimensions

Flow	Defect Circumference, mm	Defect Depth/Height Relative to $\bar{z}$, mm
D	28	+8.2
	30	+10.0
	33	−9.4
	26	−8.2
E	30	+8.5
	28	+10.4
	30	−8.2
	27	−8.5

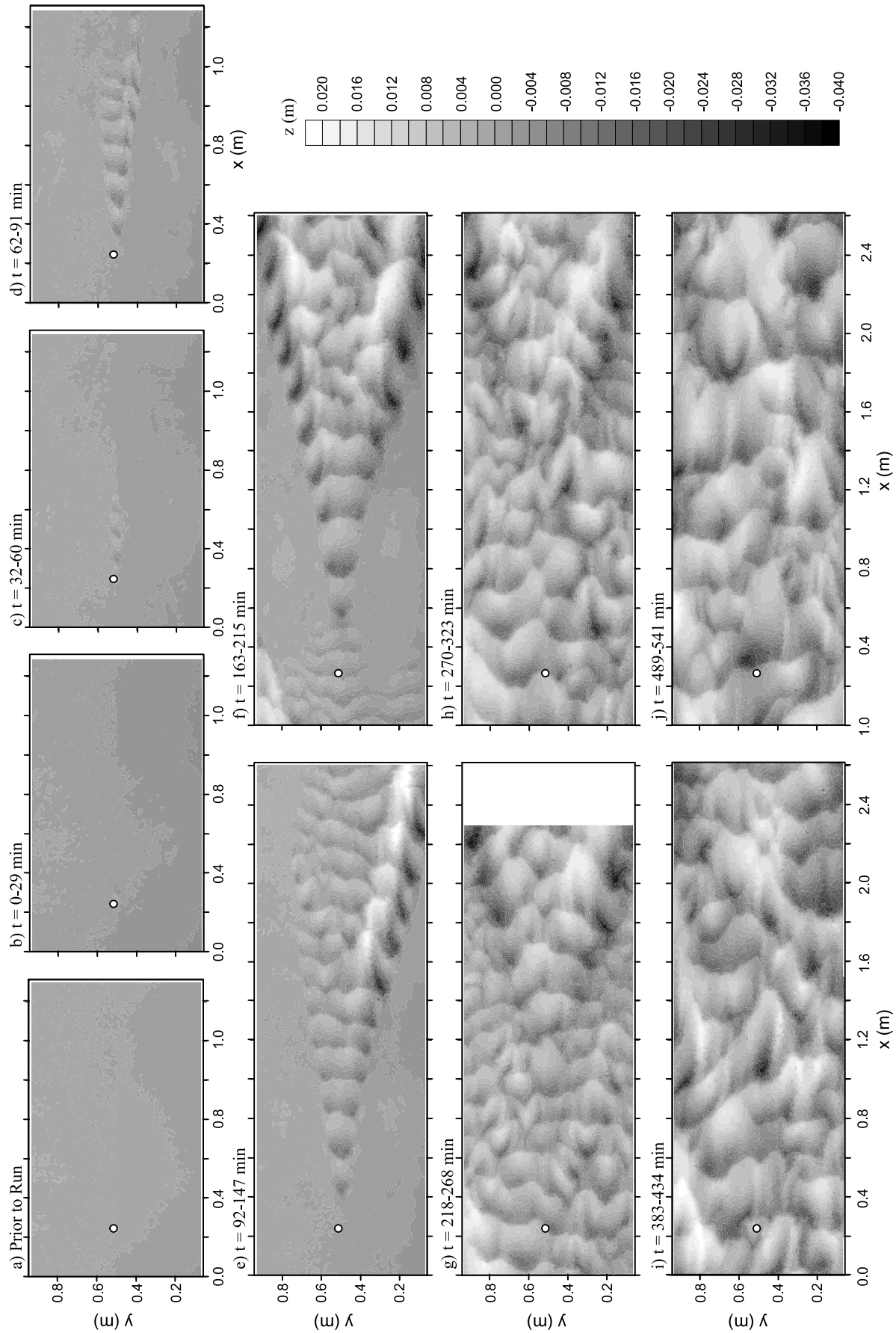
a) Prior to Run
b) t = 0-29 min
c) t = 32-60 min
d) t = 62-91 min
e) t = 92-147 min
f) t = 163-215 min
g) t = 218-268 min
h) t = 270-323 min
i) t = 383-434 min
j) t = 489-541 min
y (m)
x (m)
z (m)
0.020
0.016
0.012
0.008
0.004
0.000
-0.004
-0.008
-0.012
-0.016
-0.020
-0.024
-0.028
-0.032
-0.036
-0.040

Figure 4

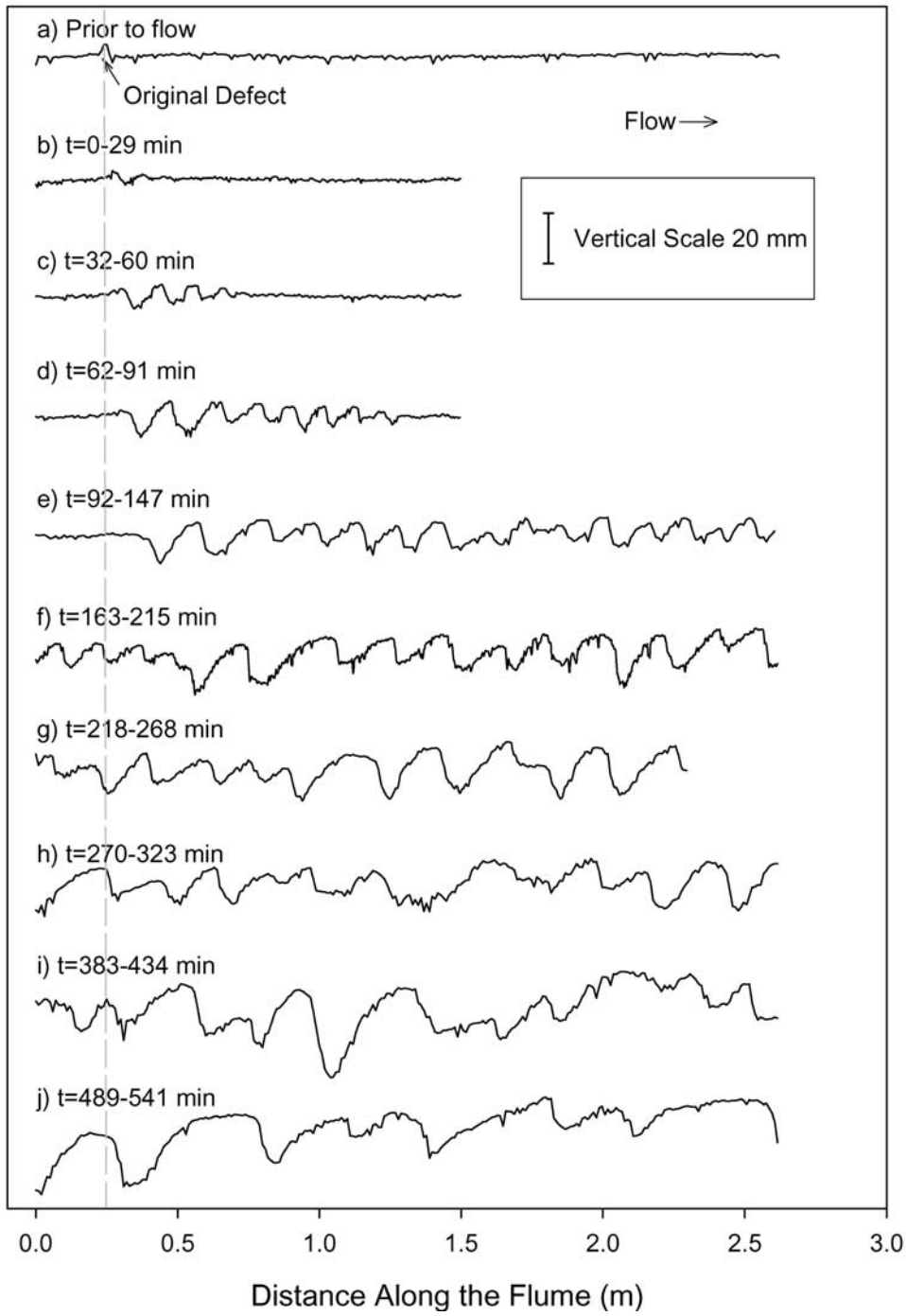

Figure 5. Cross sections drawn along the centerline of Figure 4. The map begins at 8.45 m from the head box. The dashed vertical line indicates the position of the original defect.

[33] As noted above, mapping of the bed took too much time to examine the development process in any detail and, for this purpose, the video data are examined. The way defects initially develop bed forms differs slightly between positive and negative defects and thus it is useful to describe them separately. Figure 6 shows the development of the first eight bed forms from a negative bed defect at the lowest flow strength (E) and an animation of

Figure 4. Maps of bed height as a bed form field develops from a positive defect at flow E. The initial defect dimensions are given in Table 3. The maps begin at 8.45 m from the head box. The white dot indicates the location of the original defect. Times are from the beginning of the experiment, and ranges give the time during which the bed was mapped. Flow is left to right.

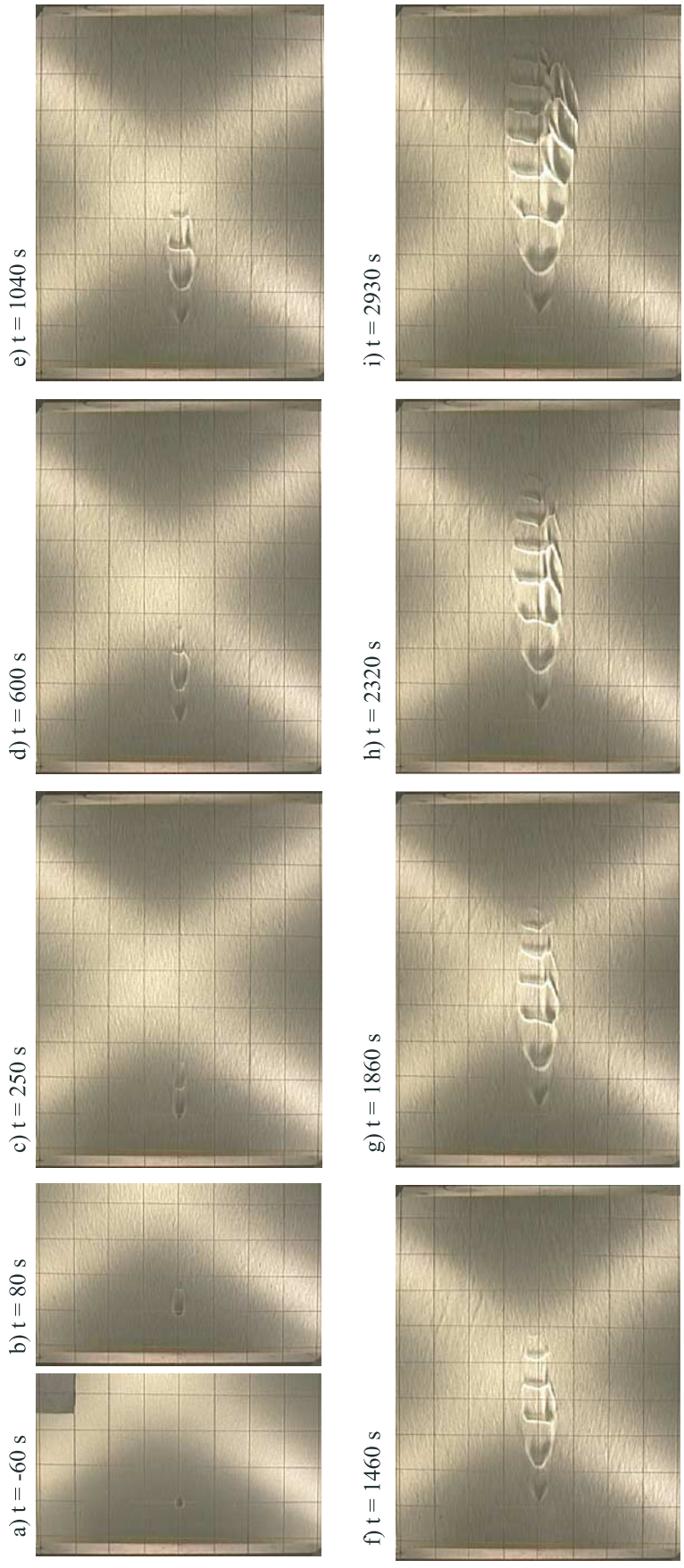

Figure 6. Evolution of bed forms from a negative defect at flow E. Prior to $t = 0$ s the discharge was being ramped up to the desired flow strength. Grid spacing is 0.115 m, and flow is left to right.

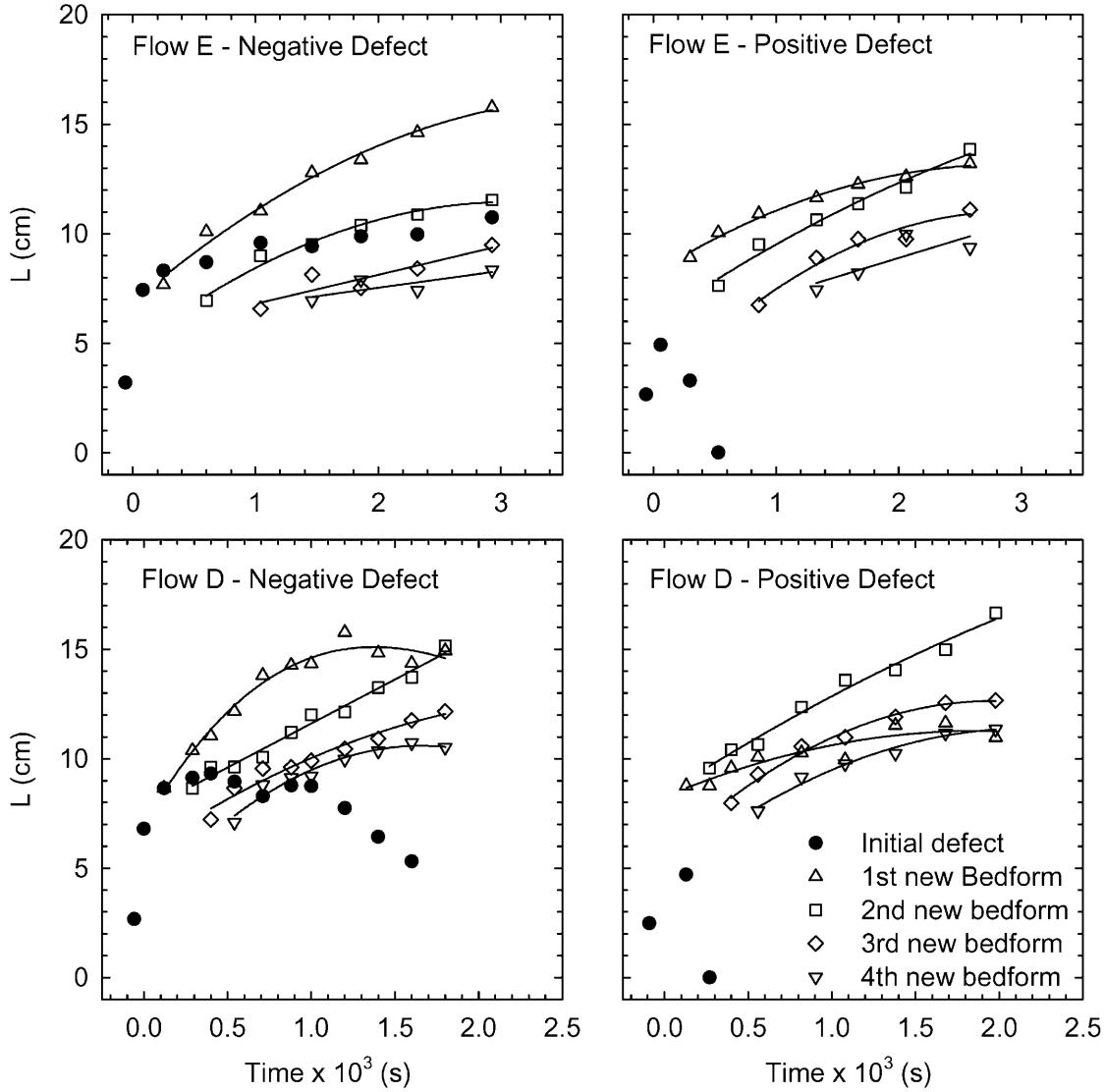

Figure 7. Bed form length L for the first five bed forms developed from negative and positive defects. The initial defect dimensions are given in Table 3.

this run is available[1]. As the flow is increased to the desired flow strength a negative defect undergoes the following deformations: (N1) initial divot extension in the downstream direction to develop a shallow scour pit (Figure 6b); (N2) sediment eroded from the scour pit begins to accumulate at the downstream edge; (N3) the edge is squared off in the cross-stream direction as in Figure 6b; (N4) erosion of the stoss slope of the new bed form, increasing the height of the crest; (N5) a new shallow scour pit develops at the downstream edge of the new bed form crest (Figure 6c); (N6) steps N2–N5 are repeated to propagate the feature downstream, forming new bed features (Figures 6d–6i).

[34] Concurrent with this process, the original defect formed a chevron shape rather than developing into a bed form (Figure 6d). New incipient bed features tended to have crests that were narrow in their cross-stream extent for the first few crests (Figures 6c–6f), but these widened transversely, grew in height, and lengthened in the streamwise direction with time. As the upstream crests became wider, so did the subsequent forms. Once the field grew to include five new crests, the whole field began to migrate downstream. This initial stability of the bed form field was also observed at flow strength D, although the migration of the bed form field began after only two new bed forms appeared. It is likely that migration begins when the bed forms reach a threshold height, which would be expected to vary with the applied shear stress [see *Southard and Dingler*, 1971].

[35] Figure 7 displays bed form L along the centerline of the video of the initial defect and the first five bed forms as a function of time. The initial negative defect grew in length for a period of time and reached quasi-equilibrium. At the higher flow strength (D), L then decreased and the defect eventually disappeared as it was filled in from upstream. Each new bed form had approximately the same initial L. Unfortunately, no data on H could be practically derived

[1]Auxiliary material is available at ftp://ftp.agu.org/apend/jf/2004JF000149.

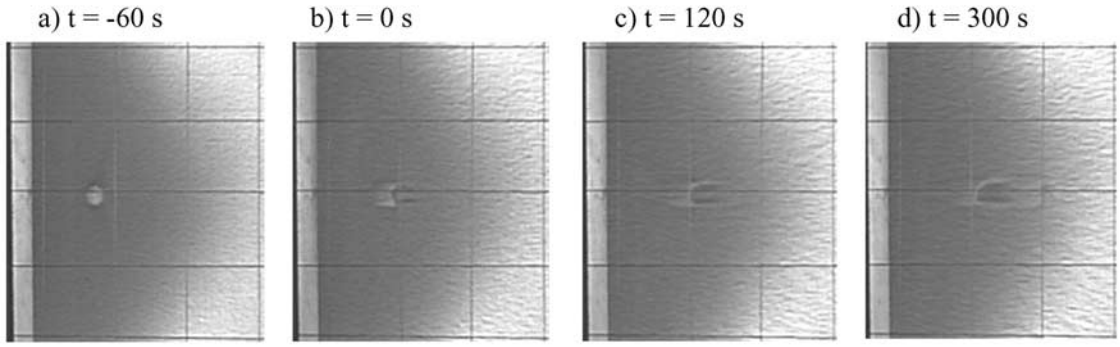

Figure 8. Evolution of a positive defect at flow strength E. Grid spacing is 0.115 m, and flow is left to right.

from the video and the maps were too infrequent to extract detailed information.

[36] The development of a bed form field from a positive defect appears to differ in several respects. Figure 8 shows the development of the first bed feature from a positive bed defect at the lowest flow strength (E). In contrast to the process described for a negative defect, as the flow is increased to the desired flow strength, a positive defect undergoes the following deformations: (P1) erosion of the stoss side of the initial defect, downstream extension, and streamlining the feature (Figure 8b); (P2) concurrently, the edge is squared off in the cross-stream direction as in Figure 8b; (P3) the defect develops arms that stretch downstream forming a barchanoid feature (Figure 8c); (P4) erosion in the lee of the defect forms a scour pit between the barchan arms; (P5) once the scour pit is developed, steps N2–N5 are repeated to propagate the feature downstream forming new bed features as in Figure 8d.

[37] Once a few new bed forms develop, the initial positive defect is planed out to the mean bed elevation (Figure 7) leaving the scour pit that eventually developed into a chevron shape not dissimilar from the feature in Figures 4d–4f. This also happens to the first new bed form after the initial positive defect has disappeared, suggesting that the positive defect is important only for generating the first scour pit and that it is the scour pits that are propagated downstream rather than the crests. Scour pits seem to be more stable features than the mounds that are generated at their downstream edge. Initial growth of the bed form field from this first scour pit is similar to growth from the initial negative defect (Figure 7).

[38] Bed form fields developed from negative (Figure 9a) and positive (Figure 9b) defects at flow strength E have approximately the same form when the fields comprise five or more bed forms. The observed processes were qualitatively similar at different flow strengths, but the development was much quicker at the larger flow strength (D). Bed form fields developed from negative (Figure 9c) and positive (Figure 9d) defects at flow strength D enveloped the field of view in only 20 min compared to 45 min at the lower flow strength (E). At both flow strengths, the positive defect field was slightly more developed than the negative defect field although the development was more pronounced for the larger flow. The more rapid development of the positive defect may be attributed to the fact that there was more sediment initially available in the positive defect case. A negative defect must excavate the sediments from the scour pit initially while the positive defect offers an ample supply of sediment above the mean bed elevation in the defect itself.

[39] Most authors have argued that the erosion in the lee of the initial features, the development of the scour pit, and the propagation of the initial features is caused by the development of a flow separation cell [cf. *Raudkivi*, 1966; *Southard and Dingler*, 1971; *Best*, 1992]. A velocity profile taken just downstream of a developing negative defect at flow strength E suggests as much (Figure 10). The defect was ~10 mm deep and had a circumference of 30 mm at flow E. Profiles taken over the defect bed and over a flat bed match closely in the range z/d = 0.2 to 1. However, below z/d = 0.2, U is dramatically reduced relative to its flat bed value and U_{rms} is increased, providing the turbulent energy to scour the bed form lee. These observations support the appearance that flow separation processes drive the development of the defect field [*Raudkivi*, 1966; *Southard and Dingler*, 1971; *Best*, 1992].

[40] *Coleman and Melville* [1996] also observed defect bed form initiation noting that when θ was just above its critical value (θ_c) for entrainment based on the modified Shields curve [cf. *Miller et al.*, 1977], bed forms developed at isolated locations on the bed that propagated downstream. At larger values of θ, they observed bed form development at multiple locations on the bed before defects could propagate. This was also observed in the present experiments where, at the lowest flow strengths (D and E), θ is just above θ_c. Artificially made defects that were placed on the bed at the larger flow strengths (A, B and C) failed to persist. The defects were simply washed out and little or no remnant was observed only a few seconds after the flow was started.

6. Instantaneous Initiation Processes

[41] At flow strengths A, B, and C, bed form initiation occurred spontaneously over the entire bed surface. The development of the bed from flat to two-dimensional bed forms is documented by a series of video images (Figure 11)

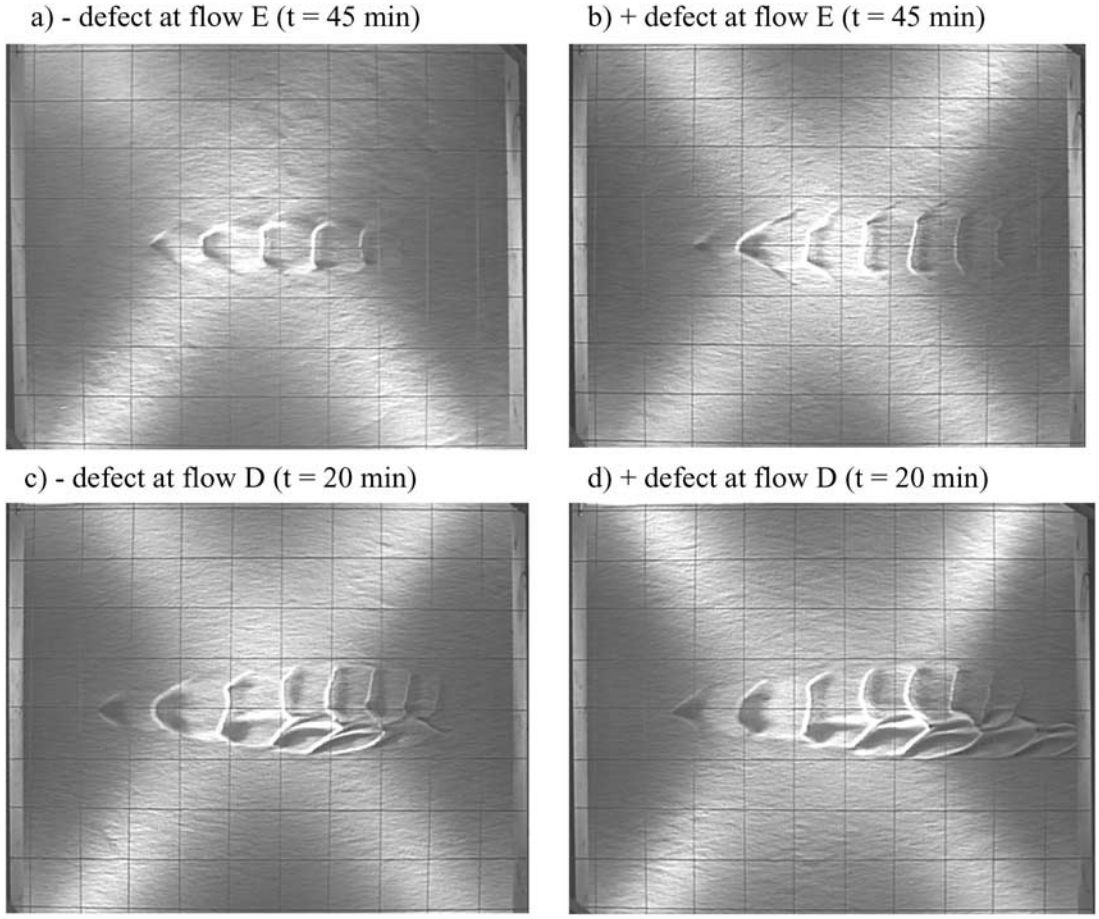

Figure 9. Positive and negative defect bed form fields developed at flow strengths D and E. Grid spacing is 0.115 m, and flow is left to right.

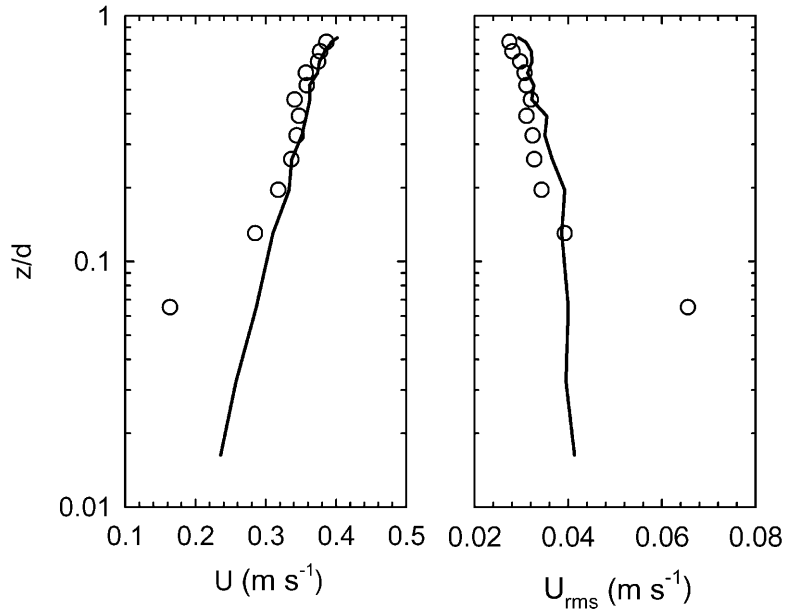

Figure 10. Profiles of mean streamwise velocity U and root-mean-square velocity U_{rms} over a negative defect and over a flat bed at flow E. Height above the bed z is normalized by the flow depth d. Open circles are data measured over the defect, and lines are profiles measured at the same flow strength without the defect.

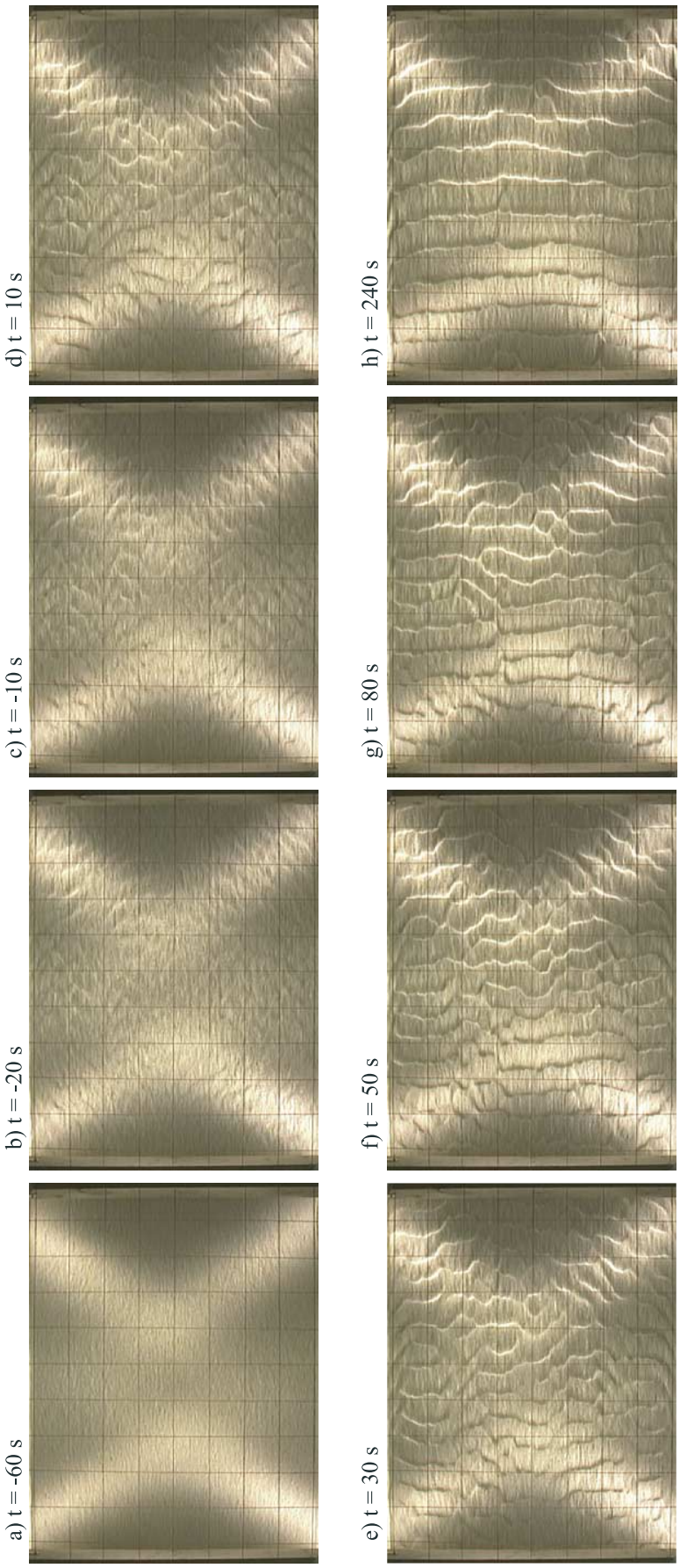

Figure 11. Evolution of a bed through instantaneous bed form initiation process at flow strength A. Prior to $t = 0$ s the discharge was being ramped up the desired flow strength. Grid spacing is 0.115 m, and flow is left to right.

and an animation of this run is available as auxiliary material. Initially, the bed was covered with lineated striations, oriented parallel to the flow, with a transverse spacing approximately equivalent to the expected streak spacing $\lambda_s = 100\nu/u_*$ (see review in *Best* [1992] and Figure 11a). These linear streaks did not appear to play any significant role in further bed development. Instead, the bed undergoes the following deformations: (1) a cross-hatch pattern is imprinted on the bed as soon as sediment begins to move (Figure 11b); (2) chevron-shaped features develop at the nodes of the cross hatch (Figure 11c); (3) chevrons begin to migrate and organize into incipient crest lines (Figure 11d); (4) crest lines straighten into two-dimensional features (Figures 11e–11h); and (5) bed forms grow in height and length (Figure 11h). The time required to move through these developmental stages decreased significantly with increasing flow strength. The full sequence illustrated in Figure 11 covers only 5 min, and the essential inception of two-dimensional bed features occurs within 100 s.

[42] The cross-hatch pattern is composed of striations at oblique angles to the flume centerline (Figure 12a). Angles between the oblique striations and the centerline ranged between 10 and 70°, with a mean between 35° and 40° for all three instantaneous initiation runs. The oblique striations were ~1 to 2 D in height. *Williams and Kemp* [1971] have indicated that flow separation occurs when

$$Re = u_* H/\nu > 4.5. \tag{12}$$

Even when $H = D$, $Re > 4.5$ and therefore it is likely that some flow separation occurred over the striations.

[43] Visual observations and video records show the cross-hatch pattern covered the entire bed of the flume. It is difficult to measure the oblique striation spacing, as the pattern is somewhat obscure outside the light paths in the images that were grabbed from the video. This is not an indication that the cross hatch was not present, but represents a limitation of the observation techniques. Where the oblique striations were well represented on the grabbed images, their separation L_{xy} was ~0.045 to 0.048 m (Table 4). Assuming the cross-hatch angles were ~35° to 40°, the streamwise separation of the nodes is ~0.064 to 0.067 m. Both separations are $\gg\lambda_s$. It can be argued that the separation could be caused by groups of streaks [cf. *Best*, 1992]. However, the cross hatch is a regular feature and it is unlikely that its origin could be linked to grouped streaks that tend to occur in patches on the bed.

[44] Once the cross-hatch pattern developed, it began to migrate downstream and formed chevron-shaped defects at the nodes of the cross hatch (Figure 12b). These chevron shapes had a developing crest line that flared upstream. Similar features have been identified by *Gyr and Schmid* [1989] when the flow strength was increased quickly and the chevron shapes are also remarkably similar to rhomboid ripple marks (see discussion in *Allen* [1982]). These features are commonly found on steep seaward-facing beaches or on bar faces where flow is shallow and temporary (transient). *Allen* [1982] notes that rhomboid ripples are transitional to transverse ripples.

[45] Once chevrons were migrating, they quickly began to organize transversely, forming flow perpendicular ridges at preferred along-stream spacing (Figure 12c). These incipient bed forms grew in size, with H increasing more quickly than L (Figure 3). In fact, L remained nearly constant until the crest lines were fairly well developed and two-dimensional (Figure 11h). The initial bed form length L_i was measured when the 2-D crest lines first emerged. In the present experiments, L_i varied between 0.04 and 0.14 m and had a mode that varied between 0.08 and 0.10 m (Figure 13 and Table 4).

[46] *Coleman and Eling* [2000] measured initial bed form lengths that conform to the relation $L = 175D^{0.75}$ (originally proposed by *Raudkivi* [1997] with slightly different coefficients). For the 0.5 mm sand used in the present experiments, this relation predicts initial bed form lengths of 104 mm, similar to L_i values. Several authors [e.g., *Coleman and Melville*, 1996; *Coleman and Eling*, 2000] have observed L_i to be relatively insensitive to flow strength, but mean L_i in the present experiments showed a statistically significant decrease with increasing flow strength, as did the time required to develop the two-dimensional forms, t_i (Table 4). Further development of these initial bed forms is presented elsewhere [e.g., *Venditti*, 2003].

7. Linkage Between Flow and Instantaneous Initiation

[47] It is difficult to make confident assertions about the linkage between flow processes and instantaneous bed form initiation in the absence of spatially resolved, instantaneous flow measurements. *Gyr and Schmid* [1989] attempted to explain instantaneous initiation by linking the initial cross-hatch feature to coherent turbulent flow structures. In particular, they speculated that the cross hatch was formed by turbulent sweep events that are ubiquitous in turbulent flows and are characterized by $+u'$ and $-w'$ velocities. They noted that, in order for turbulent events to deform the entire bed, forming the chevron shapes, the events would need to be phase locked.

[48] The chevron features observed here seem to differ from those described by *Williams and Kemp* [1971] and *Best* [1992] that are characterized by flow parallel ridges, flared at their downstream edges, with small accumulations of sediment at the mouth. *Best* [1992] argued that these features were generated by coherent turbulent structures. *Grass* [1970] laid the foundation for this idea by noting that initial sediment transport is a product of "sweep" impacts on flat sediment beds. High-speed treak structures alternate with low-speed streaks in the cross-stream direction, giving rise to hairpin vortices, bursts, and sweeps. Noting a significant difference between the size of the sweep structures and the size of initial bed defects, *Best* [1992] suggested that defects are formed by multiple hairpin vortices (associated with multiple sweeps), whose size is commensurate with the size of initial defects. *Best* [1992] also noted, in fixed-bed experiments, that burst events were concentrated over flow parallel ridges.

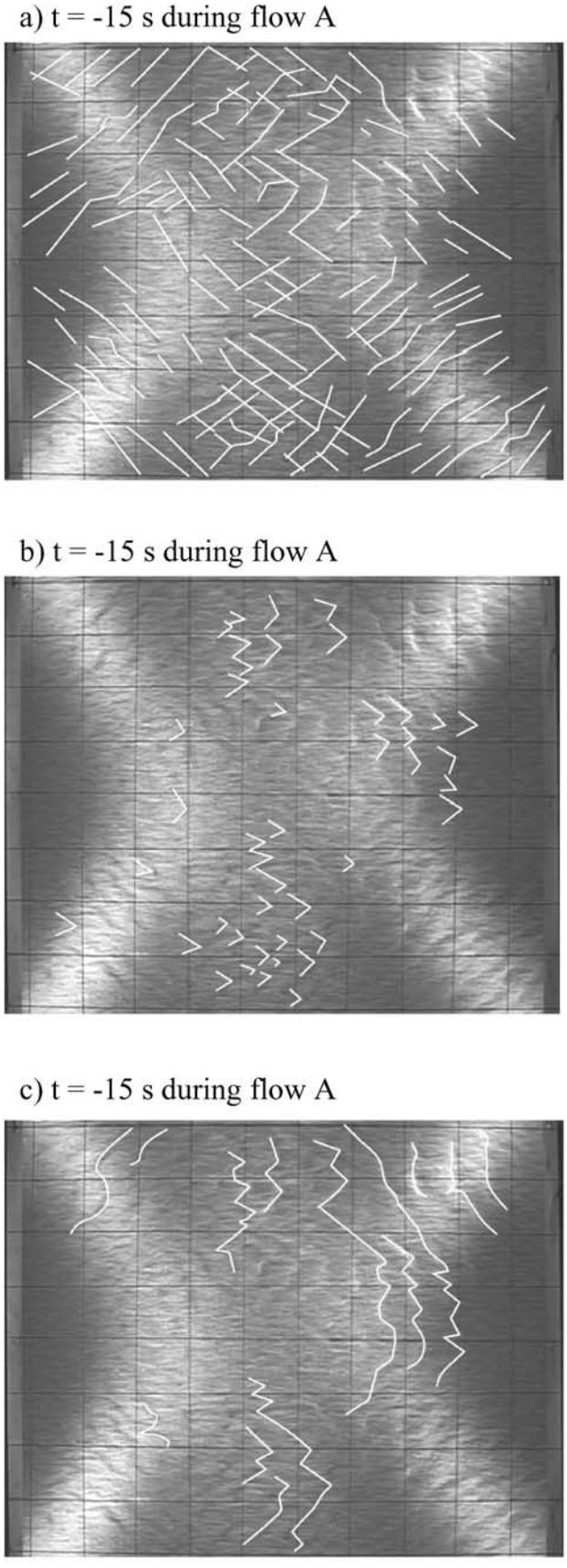

Figure 12. An example of the (a) cross-hatch patterns, (b) chevrons, and (c) incipient crest lines developed during flow A. Grid spacing is 0.115 m, and flow is left to right.

[49] While the coherent structures examined by *Grass* [1970] and *Best* [1992] may be organized, they are still considered to be random in space and time. In fact, data presented by *Best* [1992] seem to demonstrate a rather random distribution of grouped sweep structures without ridges installed in the flume. In the present experiments, lineated striations were observed on the bed, but were not coincident with the scaling of the cross hatch or chevrons. In the absence of significant flow parallel ridges, it is not clear how sweep events could become phase locked and produce the cross-hatch or chevron pattern.

[50] The origin of the cross-hatch pattern and the subsequent chevrons is an issue open to debate. However, there must be a mechanism that is responsible for their organization into linear crest lines. In order to further explore the linkage between the flow structure and instantaneous bed form development, the integral scales of the flow were calculated for the near-bed velocity measurements. Autocorrelations for the velocity time series were derived to determine integral timescales and length scales in the near bed region using the 600 s time series collected at 5 mm above the bed. An integral timescale is the time an eddy requires to pass a given point in the flow, and an integral length scale is the characteristic eddy dimension. The Eulerian integral timescale T_E is defined as

$$T_E = \int_0^k R(t)\mathrm{d}t, \tag{13}$$

where $R(t)$ is the autocorrelation function, dt is the lag distance, and k is the time step at which $R(t)$ is no longer significantly different from zero [*Tennekes and Lumley*, 1972]. With a *Taylor* [1935] approximation, the Eulerian integral length scale L_E is defined as

$$L_E = T_E \cdot U, \tag{14}$$

where U is measured at-a-point.

[51] Calculation of autocorrelations required that linear interpolation be used to convert the time series to regularly spaced events. A sampling frequency of 75 Hz was selected for the new time series as that was the minimum observed file-averaged sampling frequency for the 600 s time series. Mean and rms velocities were nearly identical between the regular and irregular time series. Each 600 s time series was divided into five 120 s sections that were detrended. Calculating autocorrelations based on these shorter sections reduces the effects of nonstationarity in the time series and, ultimately, averaged estimates of the integral scales have less associated error because the sample size is larger.

[52] In general, $R(t)$ approached zero asymptotically. In those cases when $R(t)$ approached and then oscillated about a zero value, k was determined when $R(t) = 0.01$. Table 5 presents the average streamwise T_E and L_E. Integral timescales do not vary greatly with flow velocity. Mean T_E varied between 0.23 and 0.27 s while mean L_E varied between 0.0620 and 0.0758 m. Thus in the near bed region, the average or dominant eddy size is $\sim$0.07 m or 0.5 d.

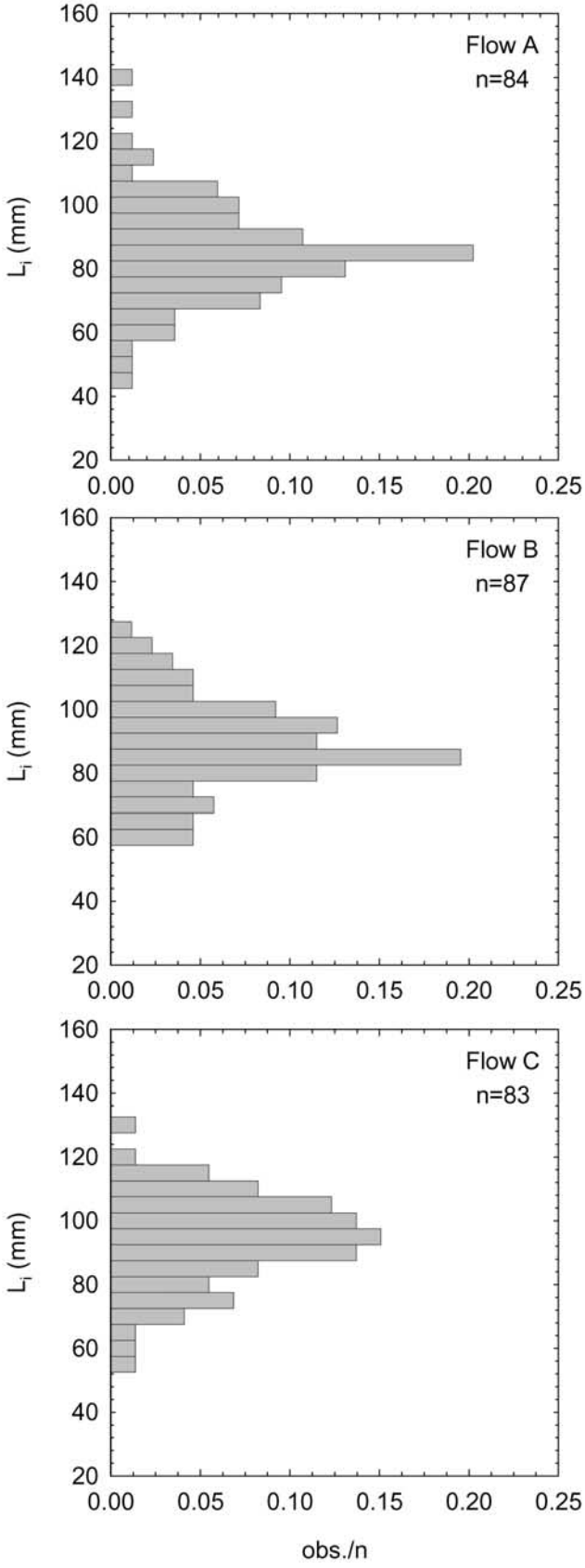

Table 4. Initial Bed Form Length Scales for Instantaneous Development Runs[a]

Parameter	Flow A	Flow B	Flow C
L_{xy}, mm	45.1	48.4	46.9
t_i, s	60	120	330
$\overline{L}_i$, mm	82.7	85.6	90.8
σL_i, mm	16.3	14.5	14.7
$L_{i-\max}$, mm	137.8	120.8	125.3
$L_{i-\min}$, mm	42.7	56.4	51.8

[a]The separation between the oblique striations L_{xy} is measured from one image at the beginning of the run and L_i is measured from a single image taken at time, t_i.

[53] This result suggests that the initial bed form lengths are slightly longer than the average eddy size that existed before the bed forms developed. Alternatively, this integral scale can indicate the length at which there are variations in velocity or shear stress. Discussions of bed form development have largely ignored the possibility that, at the earliest stage of development, bed form organization may simply be a manifestation of preexisting, wave-like variations in the bed shear stress. However, the literature is not devoid of reference to this possibility. *Gilbert* [1914] was first to suggest that bed form initiation is related to "rhythms in the flow of water and turbulence," a view widely held by scientists from the former Soviet Union [*Allen*, 1968, p. 133]. On the basis of Helmholtz's principle of "least work," *Bucher* [1919] held that bed forms are formed to afford a surface of least friction. Helmholtz's concept was later refined to explain the periodic disruption of a stratified fluid interface, now known as a Kelvin-Helmholtz wave structure. Unfortunately, *Bucher*'s [1919] ideas have been deemed incorrect because the larger-scale bed forms were envisioned to be in phase with surface waves, a phenomenon now understood to be associated with the upper flow regime and antidunes [*Allen*, 1968].

[54] Later work by *Liu* [1957] resurrected the idea of bed forms generated by a preexisting fluid flow condition by applying theory for an instability generated at the interface of a density stratified fluid. The instability was envisioned to occur at the interface of the sediment laden wall region and the viscous sublayer region of a turbulent flow resulting in a shear layer characterized by periodic streamwise variations in velocity along the bed. Unfortunately, difficulties in measuring the velocities and densities of each layer prevented *Liu* [1957] from acquiring a solution. So, the concept was extended to develop a criterion for the first appearance of bed forms based on flow variables (streamwise velocity, kinematic viscosity) and sediment characteristics (mean grain size, fall velocity). The work is largely discounted because the analysis predicts symmetric bed forms [*Allen*, 1968]. However, there is no reason to assume that an instability that gives rise to well-organized variations

Figure 13. Histograms of initial bed form wavelength, L_i, for each instantaneous initiation run. Measurements are from images at $t = 60$ s (flow A), $t = 120$ s (flow B), and $t = 330$ s (flow C). Measurements are of all bed forms on the image, from crest to crest, along the streamwise direction only.

Table 5. Integral Timescales and Length Scales[a]

Flow	$U_{0.5}$, mm s^{-1}	T_E, s	L_E, mm
A-1	285.0 ± 12.9	0.25 ± 0.03	70.4 ± 7.8
A-2	299.0 ± 11.5	0.25 ± 0.07	73.7 ± 21.4
B	280.0 ± 9.7	0.27 ± 0.04	75.8 ± 10.9
C	283.1 ± 9.1	0.23 ± 0.04	63.6 ± 10.6
D	267.2 ± 3.4	0.27 ± 0.06	71.8 ± 15.9
E	247.3 ± 5.5	0.25 ± 0.06	62.0 ± 14.4

[a]Values are mean and standard deviation of the five 120 s time series extracted from the 600 s time series.

in sediment transport must continue to dominate the flow once a bed wave is established.

8. Conclusions

[55] Bed form initiation was examined on a flat bed composed of a homogeneous 0.5 mm sand. Velocity profiles taken prior to bed form development indicate that the examined flows are typical of fully turbulent, uniform, open channel flows. Two types of bed form initiation are observed under these flow conditions: defect and instantaneous initiation. Defect initiation occurs at relatively low flow strengths, where sediment transport is patchy and sporadic, and is characterized by the propagation of defects via flow separation processes to develop bed form fields. It is widely accepted that the driving mechanism behind defect propagation is flow separation and velocity profiles taken over the defects in these experiments suggest this. Bed defects dramatically reduce the streamwise velocity near the bed, increasing turbulence and providing the turbulent energy to scour the bed form lee. However, it is still unclear how the defect is formed since, at the lower flow strengths, bed forms developed only if a defect was created artificially. These defects were quite large compared to those that might be expected to formed from turbulent flow structures in open channels. This implies that defects generated by turbulent flow structures may not be sufficient to generate bed forms, but the observations made here are too limited to draw this conclusion.

[56] At greater flow strengths, artificially formed defects simply washed away and bed forms were initiated across the entire bed spontaneously in too little time for it to be a communicated effect from the headbox. This essentially instantaneous bed form initiation has received less attention in the literature. The process begins with the imprinting of a cross-hatch pattern on the flat sediment bed, which leads to chevron-shaped forms that migrate independently of the pattern structure. The chevrons organize to form the incipient crest lines.

[57] It has been suggested that the generation of these chevrons is coherent turbulent flow structures, which seems unlikely because one must argue that spatially and temporally random events must lock in place to generate the cross-hatch pattern. Lineated striations are observed over the bed, but they are not coincident with the scaling of the cross hatch or chevrons. Integral scales measured before the onset of bed forms are $\sim 0.5\ d$ in the near bed region, which is coincident with the scale of the bed forms that later arise. Previous suggestions that bed forms arise from preexisting, wave-like structures may be valid. Spatially resolved, instantaneous flow measurements are necessary to clarify the role that turbulence plays in the initiation of bed forms.

Notation

C_{ku}, D_u line fitting coefficients.
d flow depth.
D grain size.
$ff_{0.2}$ friction factor based on a shear stress estimate from the law of the wall.
Fr Froude number.
g gravitational acceleration.
I_u streamwise turbulence intensity.
H bed form height.
$k_{s0.2}$ equivalent sand roughness based on a shear stress estimate from the law of the wall.
L, L_i bed form length and its initial value.
L_{xy} oblique striation separation.
n number of observations.
Re, Re_g Reynolds number and grain Reynolds number.
$R(t)$ autocorrelation function.
S water surface slope.
t time or experimental time.
t_i time to develop first bed form.
T_E Eulerian integral timescale.
u, u_i, U, u' streamwise velocity, its instantaneous value, its at-a-point time-averaged mean, and its fluctuation about the mean.
u_*, $u_{*0.2}$, u_{*R}, u_{*B} shear velocity, an estimate based on the law of the wall, an estimate based on Reynolds stress profile, and an estimate based on a measured Reynolds stress near the bed.
$\overline{U}$ mean flow velocity.
$U_{\max}$ maximum streamwise velocity.
U_{rms} root-mean-square of streamwise velocity.
w, w_i, W, w' vertical velocity, its instantaneous value, its at-a-point time-averaged mean, and its fluctuation about the mean.
z height above bed.
$z_{o0.2}$ roughness height based on a shear stress estimate from the law of the wall.
κ von Karman constant.
λ_s streak spacing.
ν kinematic viscosity.
θ dimensionless shear stress.
ρ_w, ρ_s density of water and sediment.
τ, $\tau_{0.2}$, τ_R, τ_B shear stress, an estimate based on the law of the wall, an estimate based on Reynolds stress profile, and an estimate based on a measured Reynolds stress near the bed.
τ_{uw} time-averaged at-a-point Reynolds stress.

[58] **Acknowledgments.** Financial support to J.V. came through a University Graduate Fellowship, a Natural Science and Engineering

Research Council of Canada (NSERC) Postgraduate Scholarship and a Research Assistantship provided through a NSERC Discovery Grant to M.C. Funds for the experiments were provided by the U.S. Department of Agriculture and NSERC. The video image frame grabber was purchased using a Ph.D. Research Grant from the American Association of Geographers–Geomorphology Specialty Group. J. Cox, J. Milam, and D. Wren at the USDA-ARS and V. Kujala at UBC provided technical support. A. Vigna helped prepare the diagrams. The journal's reviewers provided thorough critiques that have contributed significantly to the improvement of the paper.

References

Allen, J. R. L. (1968), *Current Ripples*, Elsevier, New York.

Allen, J. R. L. (1982), *Sedimentary Structures: Their Character and Physical Basis*, Elsevier, New York.

Anderson, A. G. (1953), The characteristics of sediment waves formed on open channels, paper presented at the 3rd Mid-western Conference on Fluid Mechanics, Univ. of Missouri, Missoula.

Best, J. L. (1992), On the entrainment of sediment and initiation of bed defects: Insights from recent developments within turbulent boundary layer research, *Sedimentology*, *39*, 797–811.

Bogardi, J. (1959), Hydraulic similarity of river models with movable bed, *Acta Technol. Acad. Sci. Hung.*, *24*, 417–445.

Bucher, W. H. (1919), On ripples and related sedimentary surface forms and their paleogeographic interpretation, *Am. J. Sci.*, *47*, 149–210, 241–269.

Coleman, S. E., and B. Eling (2000), Sand wavelets in laminar open-channel flows, *J. Hydraul. Res.*, *38*, 331–338.

Coleman, S. E., and B. W. Melville (1996), Initiation of bedforms on a flat sand bed, *J. Hydraul. Eng.*, *122*, 301–310.

Dantec Measurement Technology (1995), *Fiber Flow, Installation and User's Guide*, Skovlunde, Denmark.

Engelund, F. (1970), Instability in erodible channels, *J. Fluid Mech.*, *42*, 225–244.

Fredsoe, J. (1974), On the development of dunes in erodible channels, *J. Fluid Mech.*, *64*, 1–16.

Gilbert, G. K. (1914), The transport of debris by running water, *U.S. Geol. Surv. Prof. Pap.*, *86*, 263 pp.

Grass, A. J. (1970), Initial instability of fine sand, *J. Hydraul. Div. Am. Soc. Civ. Eng.*, *96*, 619–632.

Gyr, A., and A. Schmid (1989), The different ripple formation mechanism, *J. Hydraul. Res.*, *27*, 61–74.

Kennedy, J. F. (1963), The mechanics of dunes and anti-dunes in erodible channels, *J. Fluid Mech.*, *16*, 521–544.

Kuru, W. C., D. T. Leighton, and M. J. McCready (1995), Formation of waves on a horizontal erodible bed of particles, *Int. J. Multiphase Flow*, *12*, 1123–1140.

Leliavsky, S. (1955), *An Introduction to Fluvial Hydraulics*, Constable, London.

Liu, H.-K. (1957), Mechanics of sediment-ripple formation, *J. Hydraul. Div. Am. Soc. Civ. Eng.*, *83*, 1–23.

Lyn, D. A. (1993), Turbulence measurements in open-channel flow over bedforms, *J. Hydraul. Eng.*, *119*, 306–326.

McLean, S. R. (1990), The stability of ripples and dunes, *Earth Sci. Rev.*, *29*, 131–144.

Menard, H. W. (1950), Sediment movement in relation to current velocity, *J. Sediment. Petrol.*, *20*, 148–160.

Miller, M. C., I. N. McCave, and P. D. Komar (1977), Threshold of sediment motion under unidirectional currents, *Sedimentology*, *24*, 507–527.

Nelson, J. M., R. L. Shreve, S. R. McLean, and T. G. Drake (1995), Role of near bed turbulence structure in bed load transport and bed form mechanics, *Water Resour. Res.*, *31*, 2071–2086.

Nezu, I., and H. Nakagawa (1993), *Turbulence in Open-Channel Flows*, A. A. Balkema, Brookfield, Vt.

Nezu, I., and W. Rodi (1986), Open-channel flow measurements with a laser Doppler anemometer, *J. Hydraul. Eng.*, *112*, 335–355.

Raudkivi, A. J. (1963), Study of sediment ripple formation, *ASCE J. Hydraul. Div.*, *89*, 15–33.

Raudkivi, A. J. (1966), Bedforms in alluvial channels, *J. Fluid Mech.*, *26*, 507–514.

Raudkivi, A. J. (1997), Ripples on a streambed, *J. Hydraul. Eng.*, *123*, 58–64.

Simons, D. B., and E. V. Richardson (1961), Forms of bed roughness in alluvial channels, *Trans. Am. Soc. Civ. Eng.*, *128*, 284–302.

Smith, J. D. (1970), Stability of a sand bed subjected to a shear flow of low Froude number, *J. Geophys. Res.*, *75*, 5928–5940.

Southard, J. B., and J. R. Dingler (1971), Flume study of ripple propagation behind mounds on flat sand beds, *Sedimentology*, *16*, 251–263.

Sukhodolov, A., M. Thiele, and H. Bungartz (1998), Turbulence structure in a river reach with sand bed, *Water Resour. Res.*, *34*, 1317–1334.

Taylor, G. I. (1935), Statistical theory of turbulence: Parts 1–4, *Proc. R. Soc. London, Ser. A*, *151*, 421–511.

Tennekes, H., and J. L. Lumley (1972), *A First Course in Turbulence*, MIT Press, Cambridge, Mass.

van Rijn, L. C. (1993), Principles of sediment transport in rivers, estuaries and coastal seas, Aqua, Amsterdam, Netherlands.

Venditti, J. G. (2003), *The Initiation and Development of Sand Dunes in River Channels*, Ph.D. thesis, Univ. of Br. Columbia, Vancouver, Canada.

Williams, P. B., and P. H. Kemp (1971), Initiation of ripples on a flat sand bed, *J. Hydraul. Div. Am. Soc. Civ. Eng.*, *97*, 505–522.

Yalin, M. S. (1992), *River Mechanics*, Elsevier, New York.

S. J. Bennett, Department of Geography, 112 Wilkeson Quad, University at Buffalo, Buffalo, NY 14261-0055, USA. (seanb@buffalo.edu)

M. A. Church, Department of Geography, University of British Columbia, #217-1984 West Mall, Vancouver, British Columbia, Canada V6T 1Z12. (mchurch@geog.ubc.ca)

J. G. Venditti, Department of Earth and Planetary Sciences, 307 McCone Hall, University of California, Berkeley, CA 94720-4767, USA. (jgvenditti@yahoo.ca)